The application of MEMS seismometers to regional-scale passive seismology: a case study of the Sercel WiNG nodes.

Tobermory Mackay-Champion[1], Thomas Hudson[2], Nicholas Harmon[3], Chris Ogden[4], Steve Wilcox[5], Lucy Finch[6], Victoria Lane[6], John-Michael Kendall[1], and Michael C. Daly[1]

[1]*Department of Earth Sciences, University of Oxford, South Parks Road, Oxford, UK*
[2]*Institute of Geophysics, ETH Zürich, Switzerland*
[3]*Geology and Geophysics, Woods Hole Oceanographic Institution, Woods Hole, Massachusetts 02543, USA, Woods Hole Oceanographic Institute, USA*
[4]*School of Geography, Geology and the Environment, University of Leicester, Leicester, UK*
[5]*retired from Sercel*
[6]*SEIS-UK, University of Leicester, Leicester, UK*

Corresponding author:
Tobermory Mackay-Champion, tmackaychampion@gmail.com
https://orcid.org/0000-0002-6132-3327

Author Contribution Statement

Tobermory Mackay-Champion: Conception or design of the study. Acquisition, curation, analysis, or interpretation of data. Design and validation of methods and results.

Thomas Hudson: Conception or design of the study. Acquisition, curation, analysis, or interpretation of data. Design and validation of methods and results.

Nicholas Harmon: Acquisition, curation, analysis, or interpretation of data. Design and validation of methods and results.

Chris Ogden: Acquisition, curation, analysis, or interpretation of data. Design and validation of methods and results.

Steve Wilcox: Acquisition, curation, analysis, or interpretation of data.

Lucy Finch: Acquisition, curation, analysis, or interpretation of data.

Victoria Lane: Acquisition, curation, analysis, or interpretation of data.

John-Michael Kendal: Conception or design of the study. Acquisition, curation, analysis, or interpretation of data.

Michael C. Daly: Conception or design of the study. Acquisition, curation, analysis, or interpretation of data.

Abstract

Micro ElectroMechanical Systems (MEMS) accelerometers have become increasingly common in geophysical studies. Despite this, no work has been done to assess the suitability of an array of MEMS sensors to low-frequency, regional-scale passive seismic studies. Consequently, a month's-long deployment of twenty MEMS-based Sercel WING nodes, two Güralp CMG-ESPCDS and one 4.5 Hz geophone-Reftek system was undertaken to assess the performance of MEMS accelerometers in comparison to conventional seismometers. We show that the WiNG nodes reliably record over 100 Hz to 0.03 Hz, with a -136 dB broadband noise-floor between 100 – 1 Hz, and a 1/*f* noise-floor at frequencies below 1 Hz. The nodes accurately recorded earthquakes with epicentral distances ranging from 72°to 40 km. In particular, the low-period (c. 10 - 30s) surface waves of two teleseismic earthquakes were clearly resolved above the WiNG node's noise floor. A set of three WiNG nodes deployed in a 3-component configuration provided an estimate of the crustal thickness beneath Oxford of 39.0 ± 2.0 km using the H-k stacking technique. This compares favourably with the estimate provided by the conventional 3-component ESPCD (37.9 ± 1.3 km) and aligns well with previous results in the literature. The MEMS-based systems have a number of clear advantages over conventional systems, including speed of deployment, cost, small size. The strong performance of the WiNG nodes during this study shows that these MEMS-based accelerometers are well-suited for passive seismology at a local, regional, and potentially larger scale.

1 Introduction

Since the early 2000s, Micro ElectroMechanical Systems (MEMS) accelerometers have become increasingly common in geophysical studies, particularly within the field of seismic exploration for hydrocarbons (e.g.,Laine and Mougenot, 2007). Conventional seismometers, such as geophones, rely on a force-feedback system in which an internal mass moves in response to ground motion. This movement induces a voltage which is proportional to the ground motion. Closed-loop MEMS sensors, as opposed to open-loop which demonstrate poorer bandwidth, rely on force-balance systems which work by recording the voltage required to keep a positive electrode stationary between a pair of negative electrodes (Herrmann et al., 2021 Liu et al., 2022;). These sensors record in units of acceleration, which can be readily equated to force. MEMS sensors have a number of advantages over conventional instruments: their lightweight and compact design makes deploying large arrays easier, the instrument sensitivity to external factors such as temperature are an order of magnitude less than standard geophones (Laine and Mougenot, 2014), the sensors lack the data jitter seen in geophones (Herrmann et al., 2021), and the instrument response in acceleration is constant across the frequency domain (Tellier et al., 2020). The MEMS sensors have been widely used in a number of different fields, from regional-local earthquake detection (e.g., d'Alessandro et al., 2014) and the monitoring of local seismic risk using dense arrays (e.g., Fulawka et al., 2022), to Martian seismology on the NASA InSight Mission (Pike et al., 2014; e.g., Lognonne et al., 2020) and ocean-bottom deployments (Tellier and Herrmann, 2023). Despite this burgeoning utilisation and the proven ability of MEMS sensors to record well below 1 Hz (e.g., Fougerat et al., 2018), no work has yet assessed the suitability of an array of MEMS sensors for regional-scale passive seismic studies relying on frequencies below 10 Hz. Given the advantages listed above, MEMS sensors could pose a significant benefit to passive seismic studies if shown to have the appropriate bandwidth, noise floor and sensitivity. Consequently, we test the suitability of an array of MEMS-based nodal seismometers to regional passive seismology by comparing the results of an array of vertical-component Sercel WiNG nodes deployed in Oxfordshire, UK, to the results for two broadband seismometers (Güralp CMG-ESPCDs) and a 4.5 Hz geophone (connected to a Reftek-RT130 datalogger) which were deployed coincident to the nodes. We focus on noise characteristics of the MEMS sensors and the suitability of the array for ambient noise tomography, as well as the recovery of earthquakes and their application to crustal thickness estimates using H-k stacking of receiver functions. The Sercel WiNG nodes, deployed in partnership with Sercel and equipped with the latest Sercel MEMS technology called Quietseis, demonstrate all the requirements of a MEMS seismometer outlined by d'Alessandro et al. (2019). We therefore view them as a representative case study for the performance of MEMS-based sensors.

2 Methods

2.1 Array details

An array of 20 Sercel WiNG nodes were deployed throughout Oxfordshire between 19th October - 16th November 2020. The array was approximately 50 km long, and trended NW-SE (Figure 1). At two sites, the WiNG nodes were deployed alongside more conventional seismometers. The first site, in central Oxford, hosted a 60s - 100 Hz Güralp CMG-ESPCD and a GS-11D 4.5Hz geophone with a RefTek DAS130-01 broadband data logger, and three WiNG nodes in a 3-component configuration.

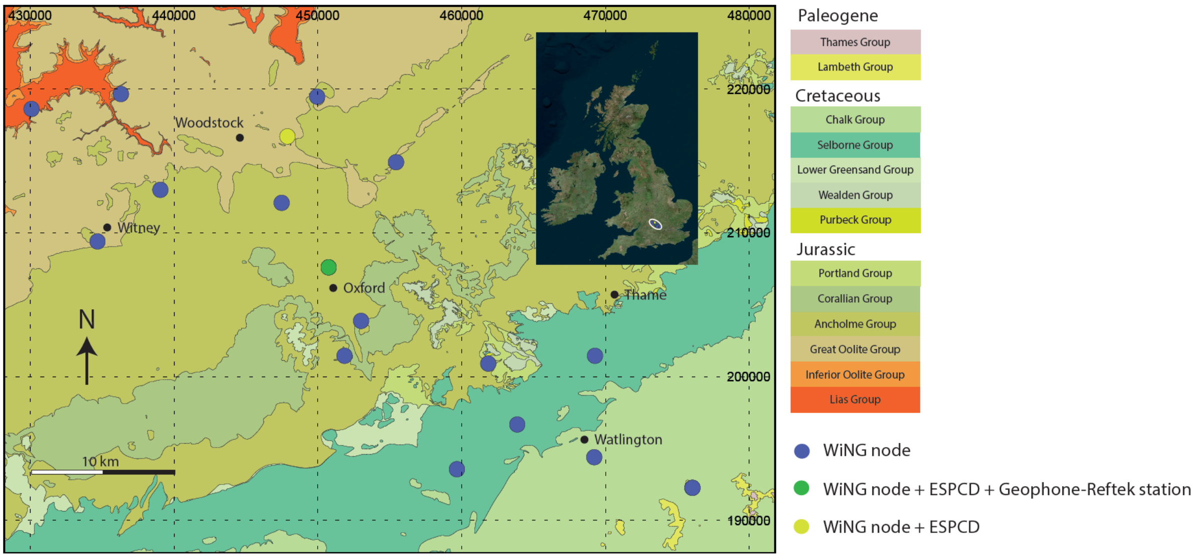

Figure 1. Deployment map. The BGS 1:50K EW236 Whitney Bedrock map is reproduced with the permission of the British Geological Survey © UKRI 2023. All Rights Reserved.

The second site in north Oxfordshire hosted a 60s - 50 Hz Güralp CMG-ESPCD and a single, vertical-component WiNG node. Both ESPCDs were directly buried, in vaults ~1m deep. The pits were backfilled with soil and sand. The geophone was also buried to a depth of ~30cm. The WiNG nodes were lightly buried such that the top of the casing was a maximum of 5cm below the surface. Unlike the geophone and the ESPCD, the WiNG nodes have an internal GPS system. Consequently, the nodes need a shallow burial to prevent loss of the GPS signal. Alternatively, the nodes can be spiked into the ground (Figure 2).

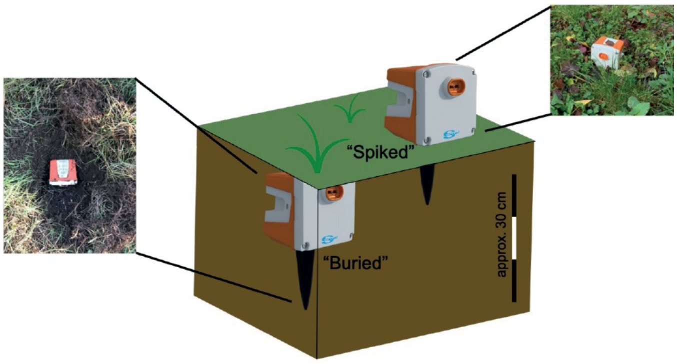

Figure 2. Deployment techniques for the WiNG nodes.

2.2 Instrument specifications and response

The Sercel WiNG nodes are vertical-component only and use a closed-loop MEMS accelerometer to record ground motion with an adjustable sampling frequency from 250 to 1000 Hz. They are approximately 750g and are fully self-contained with their own internal GPS and battery. The battery lasts between 30 - 50 days, depending on the instrument set-up. According to the manufacturers, the MEMS sensor has a constant amplitude response across the frequency domain, with a bandwidth of 0 (DC) to 400 Hz. The noise floor is purported to be 15 $\mu ms^{-2}/\sqrt{Hz}$, with a constant clip level of 5 ms^{-2}, resulting in a frequency-independent dynamic range of 128 dB. The incoming acceleration signal is recorded as a 24bit output, ranging from -2^{23} to 2^{23}. To be converted back into acceleration, this bit-value must first be converted into voltage using a scalar value unique to the array (in this case, 67 *µV/count)*. The voltage can then be converted into acceleration using the instrument's sensitivity value of 0.425 $V/ms-2$. This sensitivity correction is independent of frequency. The manufacturer states a phase accuracy of < 20 μs, which is equivalent to a frequency of

50 kHz. As such, no phase correction is required for the frequency range of interest (Figure 3A).

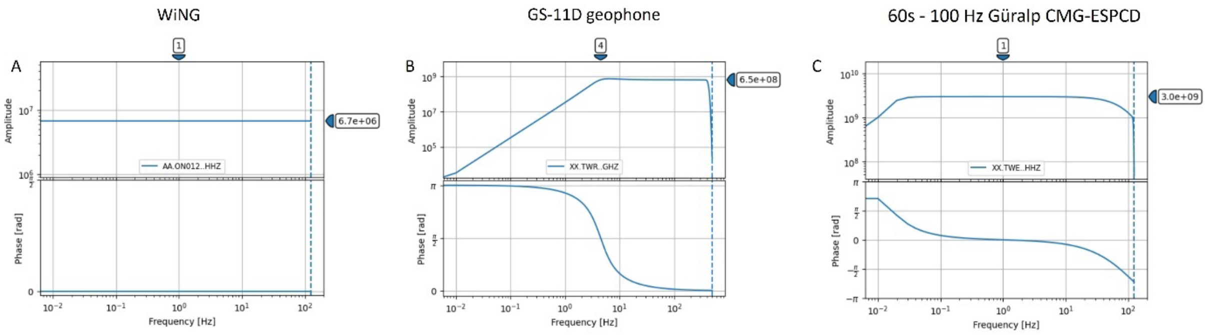

Figure 3. Instrument response Bode plot. (A) WiNG nodes. (B) GS-11D 4.5Hz geophone and RefTek DAS130-01 broadBand data logger. (C) 60s - 100 Hz Güralp CMG-ESPCD.

Two different broadband seismometers were used in the deployment: a 60s - 50 Hz Güralp CMG-ESPCD and a 60s - 100 Hz Güralp CMG-ESPCD. These instruments are conventional broadband seismometers, measuring ground velocity, which have been extensively used for passive seismology. They rely on a system of internal masses coupled with an external battery and GPS unit. These instruments have a flat response in velocity relative to frequency over the given bandwidths, and a noise-floor below the New Low Noise Model (NLNM) of Peterson (1993). The ESPCD has a sensitivity of 6000 V/ms^{-1} within the bandwidth, a clip level of 20 V (equivalent to 3.3 mms^{-1}), and a dynamic range of 165 dB at 1 Hz. Although the clip-level is lower than the WiNG node, the ESPCD have a lower noise-floor and are therefore able to attain a larger dynamic range. Like the WiNG node, the ESPCD uses a 24-bit digitizer. This digitizer has a nominal sensitivity of 1 $\mu V/count$, meaning that the total amplitude correction from counts to velocity is 3 $x10^9$ over the instrument's bandwidth. Over these frequencies, a phase correction is also required (Figure 3C).

Finally, one GS-11D 4.5Hz geophone was deployed with a RefTek DAS130-01 broadband data logger. This is a force-feedback system, with a constant frequency response above 4.5 ± 0.75 Hz. Geophones are conventionally used for monitoring frequencies above their resonant frequency and below a specific spurious frequency (Faber and Maxwell, 1997), however methods such as noise cross-correlation has been successfully applied on geophone data to yield lower frequency information (e.g., Wang et al., 2019). Below the resonant frequency, the sensitivity decays proportional to a damping factor (Havskov and Alguacil, 2016). Above its resonant frequency, the GS-11D geophone has an open-circuit sensitivity of 32 V/ms^{-1} and an open-circuit damping of 34%. The clip-level and noise floor data are not specified by the manufacturer. Like the ESPCDs, a frequency-dependent phase correction is required on the velocity data (Figure 3B).

2.3 Noise analysis and ambient noise tomography

To ascertain the potential applications of an instrument, it is crucial to understand the performance of said instrument over the frequency range of interest. For microseismic detection, frequencies between 1 - 50 Hz would be standard whereas regional to sub-regional scale surface wave analysis would require frequencies below 1 Hz. As such, the MEMS sensors need to demonstrate a wide bandwidth if they are to be of use in passive seismology. To examine this, probabilistic power spectral densities were constructed for the co-located WiNG node, ESPCD and geophone following the methodology of NcNamara and Buland (2004). First, the instrument response was removed and the ESPCD and geophone data were differentiated into acceleration. The data were then downsampled to 250 Hz, representing a factor of four for the geophone, a factor of two for the MEMS sensor and no downsampling for the ESPCD. Then the time window of interest (in this case, 1 day) was split into sliding windows of 60mins, with a 50 % overlap between windows. The Power Spectral Density, PSD, ($(ms^2)^2/Hz$) was calculated using the Welch Method for each window, and then converted into decibels relative to $1(ms^2)^2/Hz$. These are the units used by the noise models of Peterson (1993). The PSDs were then downsampled into 1/8th octave bins, and the probability was calculated following Equation 4 of McNamara and Buland (2004).

Ambient Noise Tomography (ANT), and in particular array beamforming of the cross correlations, were used to examine the frequency range of surface waves recorded by an array of WiNG nodes and to assess the suitability of the array to ambient surface wave tomography. ANT uses the phase information of cross-correlations between the ambient recordings of pairs of stations to examine the velocity structure within an array. We performed 1-bit amplitude normalisation, downsampling to 4Hz and a moving-average frequency normalisation ("spectral whitening") to the raw seismograms (Bensen et al., 2007). The seismograms for each instrument were binned into 4hr-long sections, and the cross-correlation for each station-pair was calculated for each bin. We then took a linear stack of each individual cross-correlation to create a final cross-correlation for each station pair (420 total). We only included the WiNG nodes in the analysis, as we wanted to determine their performance alone. Following stacking, we performed array-scale beamforming (following Gerstoft et al., 2006) to determine the phase velocity of waves travelling through the entire array. The average phase velocity for the array provided by this step is useful for resolving the cycle ambiguity when determining the dispersion for individual station-pair cross correlations. The phase dispersion for all station-pairs were estimated by unwrapping the phase of the Fourier transformed noise cross correlations using the average phase velocity to determine the number of cycles at the longest period. The observed phase from all useable station pairs at each period of interested was then inverted for 2-D phase velocity maps across the region using a damped, weighted least-squares following Harmon and Rychert (2016). The inversion uses a nodal parameterization, where the phase velocity at each point in the map is a weighted average of the nearby nodes. We use the average phase velocity at each period from the beamforming as our uniform starting velocity. A damping parameter of 0.2km/s was chosen based on previous work (Rychert and Harmon 2016), with a constant weighting throughout the model. To generate a shear velocity model from points of interest from the phase velocity maps, pseudo-dispersion curves at each point across the maps at all periods were generated and then inverted for S-wave velocity with depth using an iterative non-linear inversion (Rychert and Harmon ,2016; Tarantola and Valette, 1982). The inversion starting model consisted of 30 layers, each 1km thick, with an initial velocity of 4.2 km/s for each layer, following Hermann (2013). A chi-squared objective function was used, with each 1D profile achieving a value below 1, indicative of a good-fit.

2.4 Earthquake analysis

The analysis of earthquakes, on a regional and local scale, is fundamental to many techniques in seismology. MEMS sensors must reliably detect and record these earthquakes if they are to be of wide use. Teleseismic earthquakes are of particular interest, because the sensor would need to have a low enough noise floor to suitably detect highly attenuated, low frequency waves. As such, the performance of the MEMS sensors was examined for two teleseismic earthquakes (MW 7.0 from Greece, MW 7.6 from Alaska) and several more local earthquakes.

2.4.1 Arrival time analysis

Arrival time analysis, using the conventional short-term average – long-term average (STA/LTA) technique of Withers (1998), was performed on the MW 7.0 Greece earthquake, the MW 7.6 Alaska earthquake, and a MW 0.9 Stoke-on-Trent earthquake. This was done to assess the signal-to-noise ratio achieved by the MEMS sensor (proxied by the STA/LTA value), and the reliability of the MEMS sensor detection when compared to the arrival times from the ESPCDs and geophone. The conventional STA/LTA technique computes the ratio of the average absolute amplitude in the ’short time’ window against the average absolute amplitude in the ’long time’ window. A threshold ratio value is used as a ’trigger’; an earthquake arrival is ’triggered’ once the ratio value exceeds that of the pre-set threshold. The analysis was performed on acceleration data, and a suitable bandpass filter was applied prior to analysis. The frequency values used for each analysis can be found in Supplementary 1.

2.4.2 Receiver Functions

Arrivals from teleseismic earthquakes can be used to examine the crustal structure beneath the recording instrument. One such method is known as H-k stacking (Zhu and Kanamori, 2000), which uses Receiver Functions (RF) to provide an estimate of crustal thickness (*H*) and the bulk crustal V_p/V_s ratio (*k*), following Equation 1.

Equation 1

$$s(H,k) = \sum_{j=1}^{N} w_1 r_j(t_1) + w_2 r_j(t_2) - w_3 r_j(t_3)$$

Where *N* is the number of receiver functions, w_1, w_2, w_3 are stacking weightings, t_1, t_2, t_3 are the travel times of the *Ps*, *PpPs* and *PsPs+PpSs* phase respectively, and $r_j(t_i)$ are the amplitudes of the respective phases. We calculated RFs using the time-domain iterative deconvolution method of Ligorrìa and Ammon (1999), with Gaussian width factors of between 0.8 – 4.0. Receiver functions with an iterative deconvolution variance below 80 % were rejected automatically, and the remaining receiver functions were visually inspected. Following the modified H-k stacking approach of Ogden et al. (2019), which overcomes some of the parameter sensitivity issues discussed therein, we computed 1,000 individual H-k results using the calculated RFs and randomly selected input parameters for each station of interest. Cluster analysis is then used to determine the best-fitting result as well as the reliability of the result for that station. RF analysis requires 3-component systems as it involves the deconvolution of the radial component from the vertical component seismograms. Consequently, we are unable to perform RF analysis on a single node because the WiNG nodes record vertical-component information only. However, the MEMS accelerometer is not sensitive to the component direction. Therefore, we performed RF analysis on the 3C-WiNG system and compared the result to that obtained from the conventional 3-component ESPCD deployed at the same site.

3 Results

3.1 Ambient noise analysis

The Probabilistic Power Spectral Densities (PPSD) illuminate several key differences between the co-deployed 60s - 100 Hz ESPCD, 4.5 Hz geophone, and the WiNG node (MEMS sensor) (Figure 4).

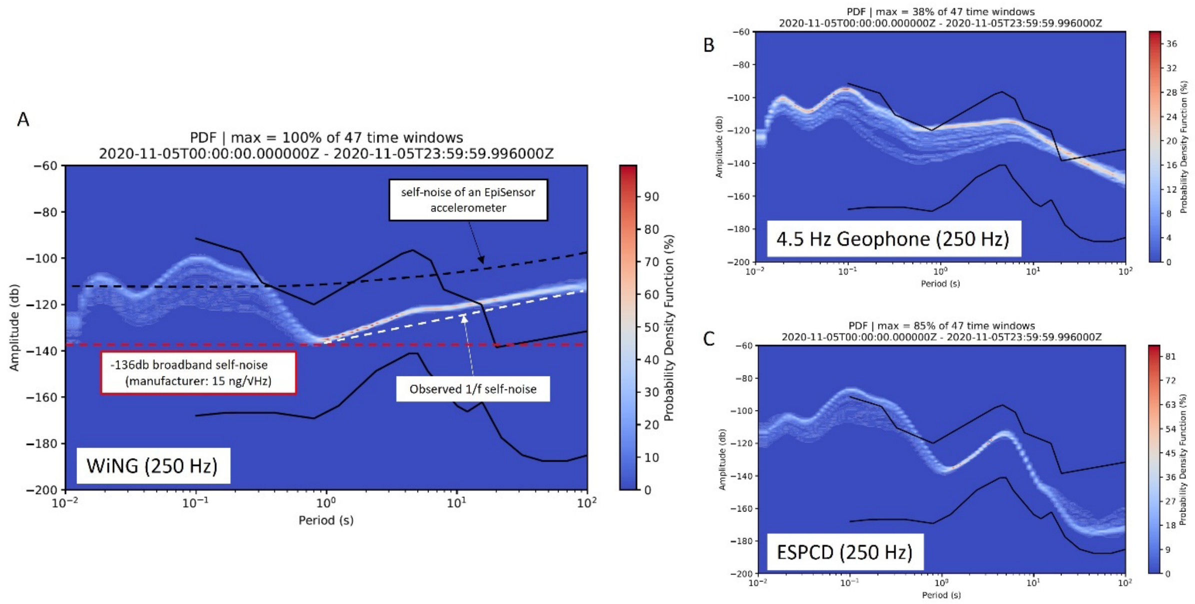

Figure 4. Probabilistic Power Spectral Density analysis on 5th November 2020. A) WiNG node. B) Geophone. C) ESPCD. Each instrument has a sampling frequency of 250 Hz in units of acceleration for this analysis. The solid black lines are the New High Noise Model (top) and New Low Noise Model (bottom) of Peterson (1993).

This site was located in central Oxford, and consequently has a high level of anthropogenic noise between 100 - 10 Hz. All of the three instruments show a similar topology between 100 - 10 Hz, with amplitudes of between -130 to -85 dB and clear peaks at approximately 90 Hz and 10 Hz. The geophone and ESPCD both show higher amplitudes throughout this frequency range, which may be due to being closer to the source of the noise or more likely to do with a higher degree of coupling with the ground. The WiNG node was buried in topsoil, which may have contributed a degree of damping of the high frequency signals, while the geophone was buried more deeply (approximately 30cm), and the ESPCD was buried even more deeply (approximately 1m). All three instruments then see a reduction in amplitude for signals between 10 to 1 Hz. The ESPCD shows an amplitude reduction of c. 70 dB and the WiNG node shows a reduction of c. 60 dB. The geophone displays a smaller change of only c. 25 dB, likely due to the geophone's resonance at 4 Hz. Nevertheless, the reduction in amplitude seen by each instrument corresponds well with the reduction seen in the New High Noise Model (NHNM) of Peterson (1993). The MEMS sensor and the ESPCD both show a tightly clustered amplitude of approximately -135 to -140 dB, and bottoms out at 1Hz. On the other hand, the geophone bottoms out at around 4 Hz, and exhibits a significant spread in amplitude from -140 dB up to -120 dB. This larger spread in amplitude no doubt corresponds to the change in behaviour of the geophone at its resonant frequency.

At periods larger than 1 s, the behaviour of the three instruments diverges. Below 1s, the WiNG node displays a broadband noise floor of 15 $\mu ms^{-2}/\sqrt{Hz}$, equivalent to a constant noise of -136dB. Signals with amplitudes below this noise floor would not be distinguishable from the background random noise of the sensor. This is some way above the New Low Noise Model (NLNM) of Peterson (1993), suggesting that the sensors would not perform well in seismically quiet areas. Above 1s, the WiNG node shows a tightly clustered amplitude with a slope of 1/*f*. This is a well-known feature of electrical circuits known as 'flicker noise' or 'pink noise' and decreases the dynamic range of the sensor at the affected periods (Sleeman et al., 2006). As with the broadband noise floor, any signal of interest would need to have an amplitude above the 1/*f* noise if it were to be adequately detected. The primary microseism at 5 - 8s is an example of such a signal, which can be clearly seen above the noise floor. The noise floor of a widely used force-balance accelerometer known as the EpiSensor is plotted for comparison, after Koymans et al. (2021). The WiNG node displays a lower noise floor, making it more suitable for passive seismology. The geophone also records the primary microseism, although the variation in amplitude of -125 to -115dB is likely caused by the resonance of the geophone and does not present variations in the primary microseism itself. This is surmised because the ESPCD displays a tight clustering of amplitude at -115 dB for the primary microseism Beyond the primary microseism, the geophone displays a linear drop in amplitude. This is indicative of a drop in sensitivity and suggests that the corner of the bandwidth has been exceeded. As already mentioned, the ESPCD displays a clear primary microseism, and a secondary microseism can also be detected at around 12- 15s. The strength of this secondary microseism clearly varies with the time window. Above 30s, the ESPCD exhibits a plateau in amplitude indicative of ’the hum’ (Kobayashi and Nishida, 1998 etc.). The amplitudes observed by the ESPCD fall well within the NHNM to NLNM window at periods above 1s and are consequently above the stated noise floor of the instrument.

3.2 Ambient Noise Tomography

The flicker noise displayed by the WiNG nodes below 1Hz is random (Halford, 1986). Consequently, cross-correlations between pairs of stations will be independent of flicker noise when stacked over a sufficient period of time. The cross-correlation of the ambient noise between the 20 station pairs creates a clear moveout of approximately 3 km/s, which is indicative of Rayleigh waves travelling through the array of WiNG nodes (Figure 5A).

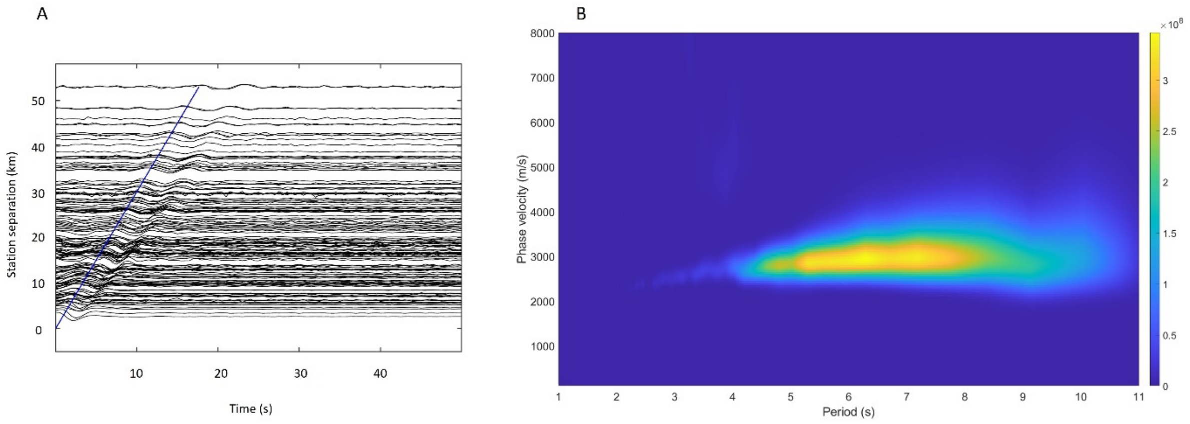

Figure 5. A) One-side cross-correlation moveout. The blue line corresponds to a velocity of 3 km/s. B) Array beamforming surface wave dispersion.

The array beamforming of these cross-correlations demonstrates that the array can detect surface waves with periods of at least 7.5s (Figure 5B). The phase velocities are all within an expected range of 2.8 - 3.5 km/s. The maximum station separation in the array is approximately 50km. Given that the phase velocity of a given surface wave can only be accurately determined if the station separation is equal to at least 2 wavelengths (Harmon et al., 2008), the 7.5 s limit was imposed on the array by the station separation. As will be shown in Section 3.3, the WiNG nodes can reliably record signals below 20 seconds.

The 2D surface-wave phase velocity maps, and associated error maps, constructed for the range of periods found in the array beamforming demonstrate that the array is detecting lateral velocity contrasts greater than the measurement error (Figure 6). The phase velocity map for a 3s surface wave (Figure 6A) shows many similarities to the geological map of Figure 2, suggesting that the detected velocity contrasts are realistic.

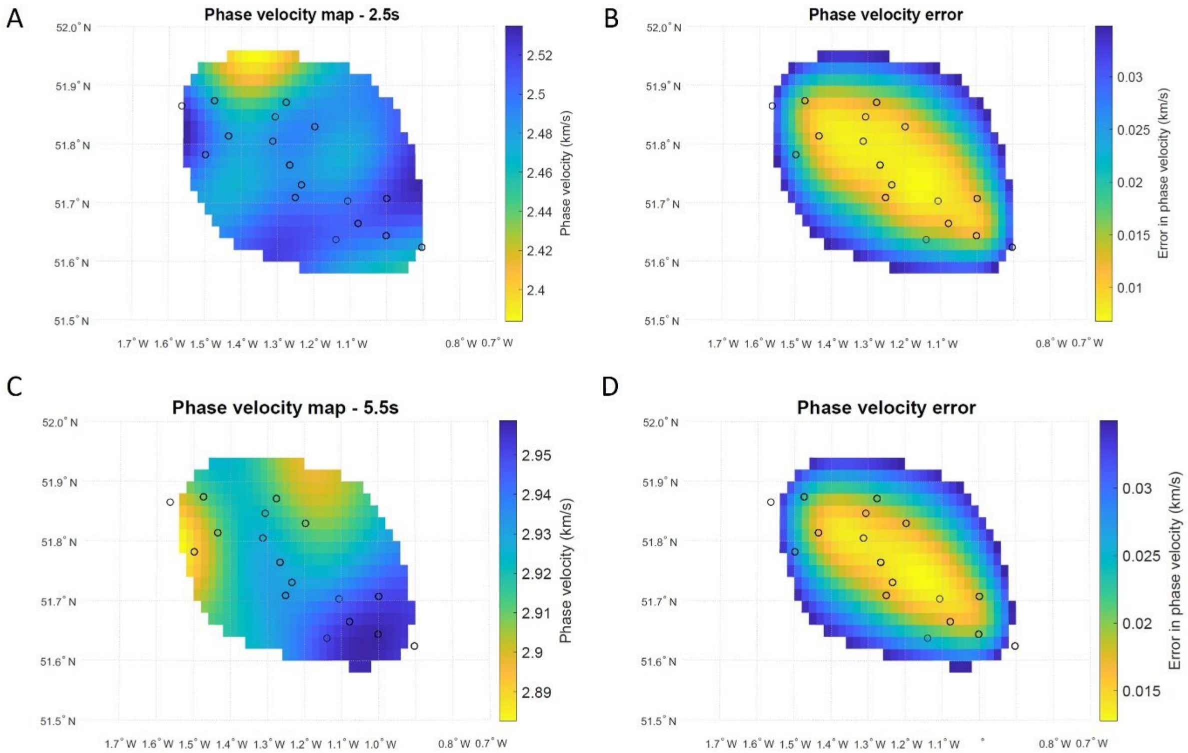

Figure 6. 2D phase velocity maps. A) Phase velocity map of 2.5s wave. B) Error in the phase velocity measurements at 2.5s. C) Phase velocity map of 5.5s wave. D) Error in the phase velocity measurements at 5.5s.

A representative surface wave dispersion curve was constructed for the profile using the phase velocity maps for each period of interest and inverted for S-wave velocity against depth (Figure 7A, B). The sensitivity of the surface waves for the period range of interest shows a peak sensitivity to depths between 2-10km, followed by a steady decline in sensitivity to a maximum depth of 20km (Figure 7C). The “best” S-wave solution comprised 4km layers with a stepwise increase in S-wave velocity, from a minimum of 2.6 km/s at the surface to a maximum of 3.9 km/s at a depth of 20 km. The large step increase in velocity below 4km likely represents the sediment-basement interface, because the outcropping geology comprises Jurassic - Paleogene lithified sediments (Woodcock & Stachan, 2012).

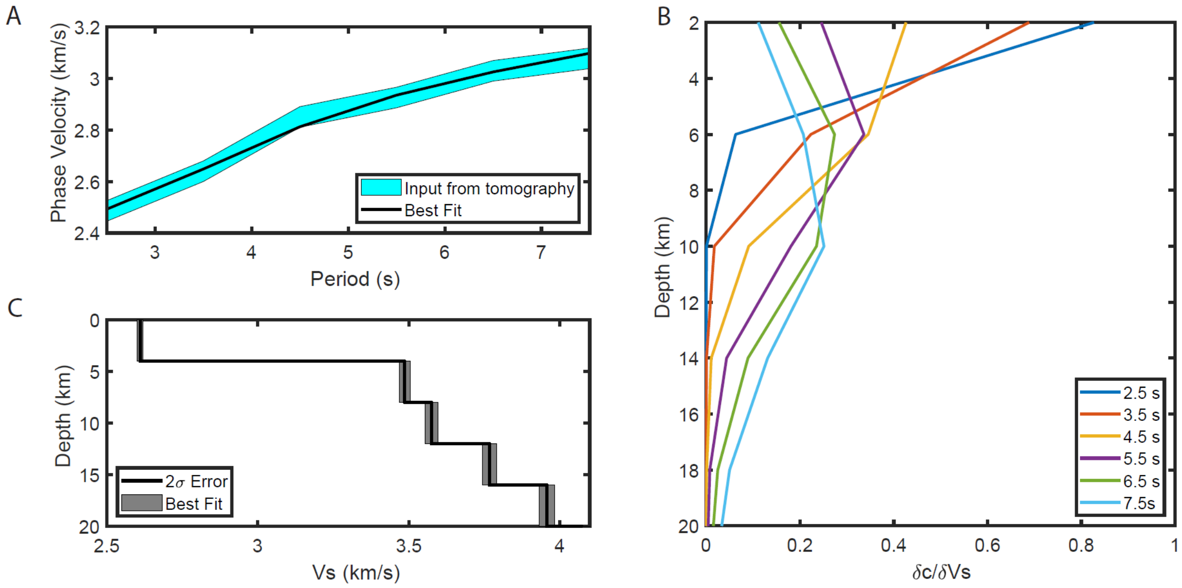

Figure 7. 1D S-wave inversion. A) The observed dispersion curve, and the forward modelled dispersion curve. B) The resulting S-wave velocity profile. C) The depth sensitivity of the surface waves used in the inversion.

3.3 Earthquake analysis

For the MEMS accelerometer to prove useful to the field of passive seismology, it must be able to detect local to teleseismic earthquakes. This provides several tests for the sensor. In particular, the low frequency arrivals associated with teleseismic earthquakes, such as the < 1Hz surface waves, must be above the 1/*f* noise floor if they are to be adequately resolved at individual stations. For more local earthquakes, the high frequency arrivals need to be resolved from the background anthropogenic noise.

A MW 7.6 earthquake from Alaska was recorded by the array on 19th October 2020, from an epicentral distance of 72 °(British Geological Survey, 2020) (Figure 8). The Power Spectral Density plot shows that both the WiNG node and the ESPCD measure a peak in amplitude at periods of 20 - 30s, corresponding to the arrival of the low period surface wave (Figure 8A). This arrival is well above the 1/*f* noise floor of the MEMS sensor so can be clearly resolved. In contrast, the geophone which shows a far broader area of increased amplitude. The lower amplitude of the WiNG node peak (-95 dB) in comparison to the peak of the ESPCD (-75dB) is likely caused by the higher quality of coupling between the ESPCD and the ground provided by the deep burial of the seismometer.

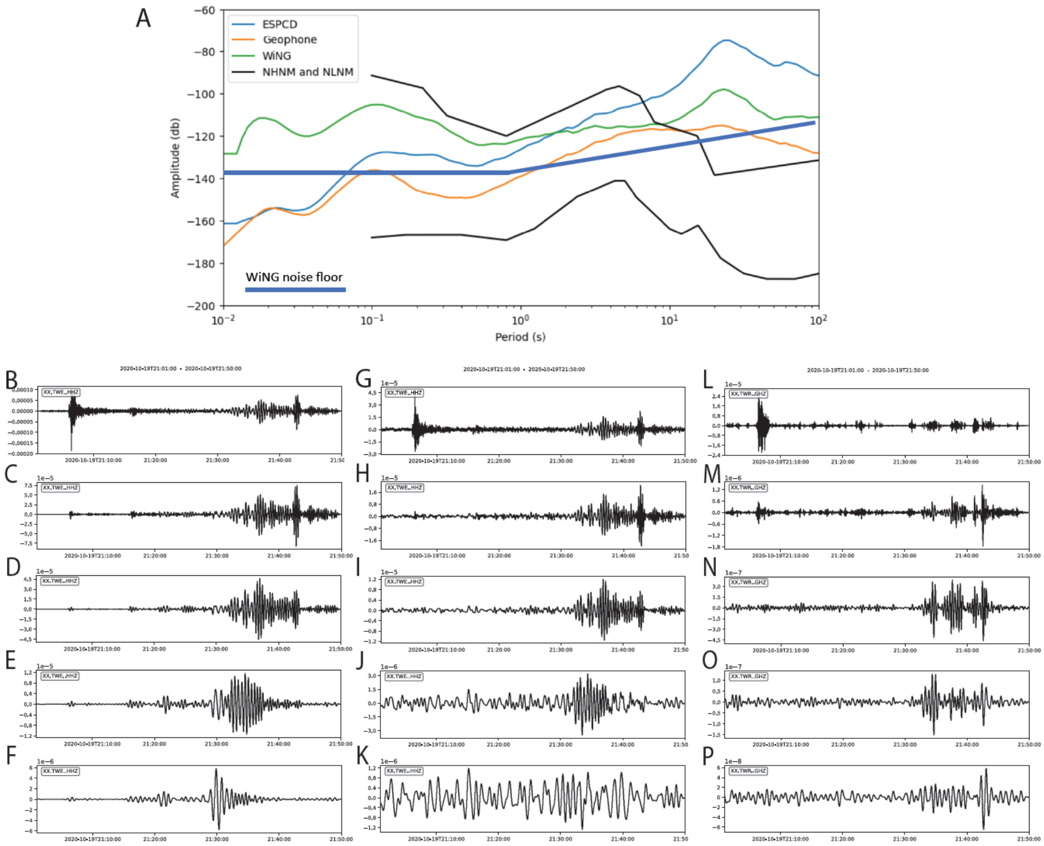

Figure 8. Instrument response to a MW 7.6 Alaska earthquake on 19th Oct. 2020. A) Instrument Power Spectral Density, in units of acceleration decibels relative to 1. (B, C, D, E, F) ESPCD acceleration data with a 1 s, 10 s, 20 s, 30 s and 40 s low-pass filter, respectively.

With a low-pass filter of 1 Hz, all three instruments show a clear P-wave arrival (Figure 8B, G, L). The surface wave train is clear in the ESPCD and WiNG record, but largely absent from the geophone data. At a low-pass filter of 10 Hz, the surface waves dominate the signal. The ESPCD and WiNG data are similar, although the WiNG node has a higher noise floor (Figure 8 C, H). The surface wave train is not smoothly recorded by the geophone, although similar arrivals can be identified (Figure 8M). The dispersion of the surface waves can be clearly observed in the WiNG and ESPCD data. For example, the arrival time of the surface wave train with a 20 Hz low-pass filter (Figure 8D) is later than the 30 Hz filter (Figure 8E), which is later than the 40 Hz filter (Figure 8F). The WiNG node reliably records signals down to 20 Hz (Figure 8I). At 30 Hz, a surface wave arrival can still be seen (Figure 8J), although the noise floor is high and some of the signal is clearly lost. No signal is observed below 40 Hz (Figure 8K). Although this performance is notably worse than the broadband ESPCD, these results show that MEMS accelerometers are capable of reliably recording low-frequency arrivals.

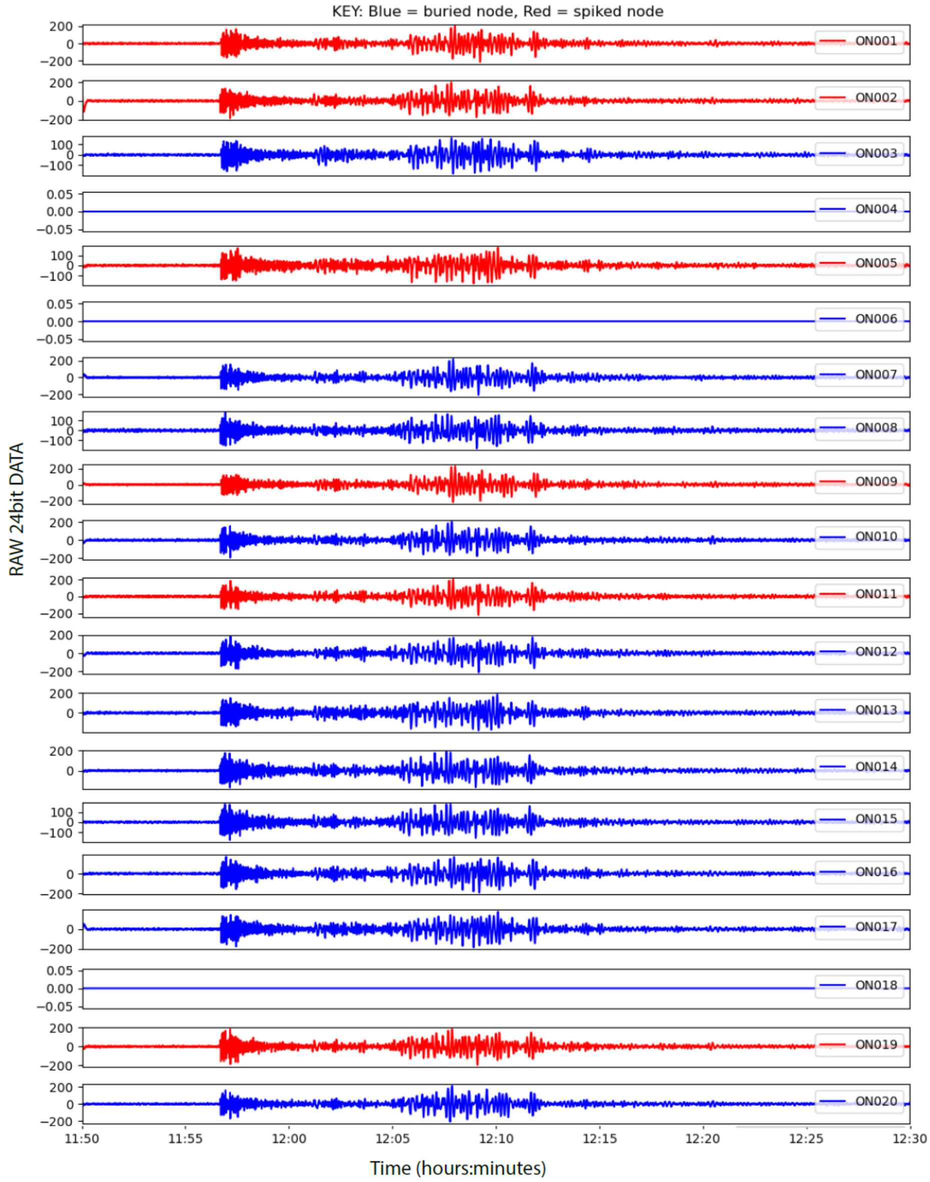

Figure 9. The response of the WiNG node array to the Greece Earthquake (MW 7.0), 30th Oct. 2020. A bandpass filter of 0.05 - 1 Hz has been applied. The blue plots correspond to nodes that were buried underground. The red plots correspond to nodes that were spiked into the ground.

The strong performance of the WiNG node at low frequencies is repeated for the MW 7.0 earthquake from Greece, which occurred at an epicentral distance of 24°(USGS, 2020). The earthquake can be clearly seen arriving at all of the deployed node stations (Figure 9). Akin to the Alaska earthquake, a clear P and surface wave arrival can be observed, and the amplitude of the arrivals is demonstrably higher than the sensor noise floor (Figure 10). The WiNG nodes also perform well in regional and local earthquakes. The MW 2.7 North Sea earthquake (epicentral distance of 6.45°(BGS,2020)) shows clear arrivals between 3 - 6 Hz (Figure 10A,B), and the low MW 0.9 Worcester earthquake (epicentral distance of 0.64°(British Geological Survey, 2020) can also be distinguished from the background noise (Figure 10D,E).

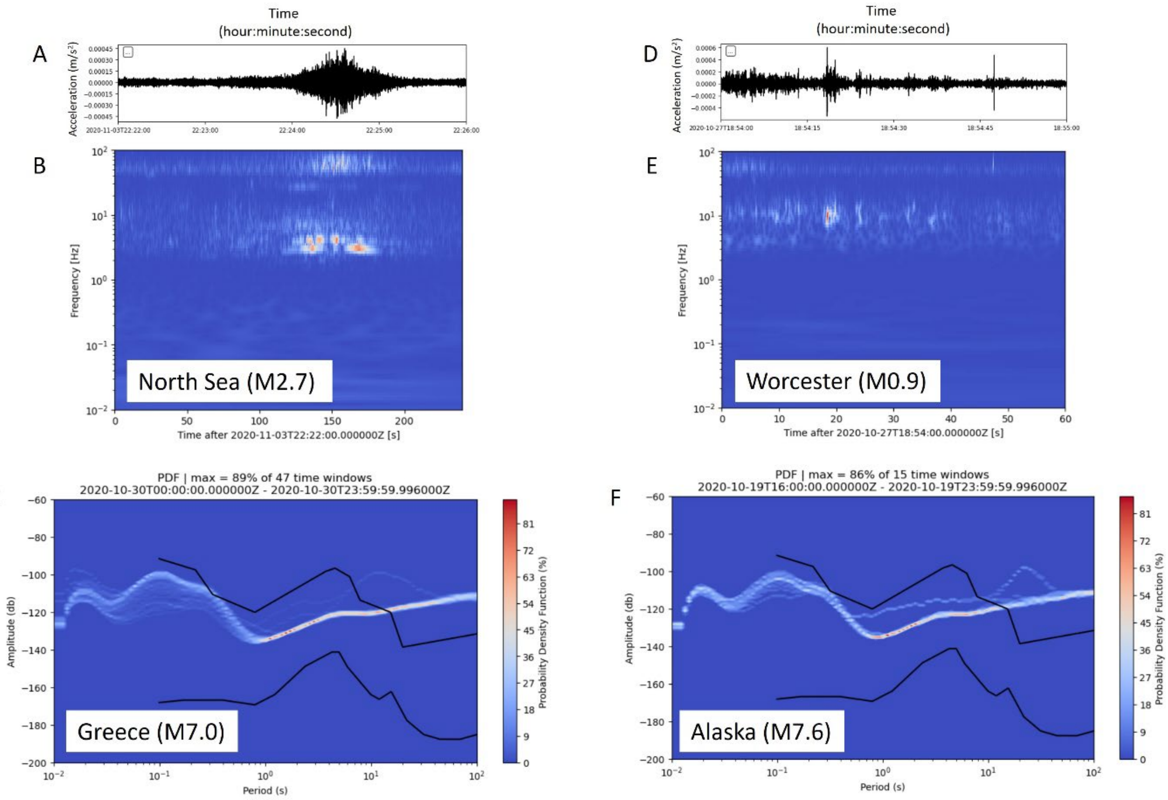

Figure 10. Response of the WiNG node to a selection of earthquakes. A) WiNG node response to the MW 2.7 North Sea earthquake; B) A continuous-wavelet-transform analysis of the North Sea earthquake. C) PPSD analysis of 30th Oct. 2020, featuring the MW 7.0 Greece earthquake; D) WiNG node response to the MW 0.9 Worcester earthquake; E) A continuous-wavelet-transform analysis of the Worcester earthquake; F) PPSD analysis of 19th Oct. 2020, featuring the MW 7.6 Alaska earthquake MW 7.6 Alaska.

3.3.1 Arrival time analysis

Arrival-time analysis was performed on a selection of regional and teleseismic earthquakes (Figure 11). For this analysis, the geophone and ESPCD data were differentiated into units of acceleration to provide a fair comparison between the instruments. This is particularly important because acceleration data features a -90°C phase shift relative to velocity. Seismograms from the ESPCDs have been plotted below the STA/LTA picks to validate the results. The first earthquake analysed was a MW 1.3 from Stoke-on-Trent, with an epicentral distance of 1.27°(British Geological Survey, 2020) (Figure 11A, B, C). As observed in the seismograms, the high noise levels of Oxford made this earthquake undetectable at many stations (Figure 11C).

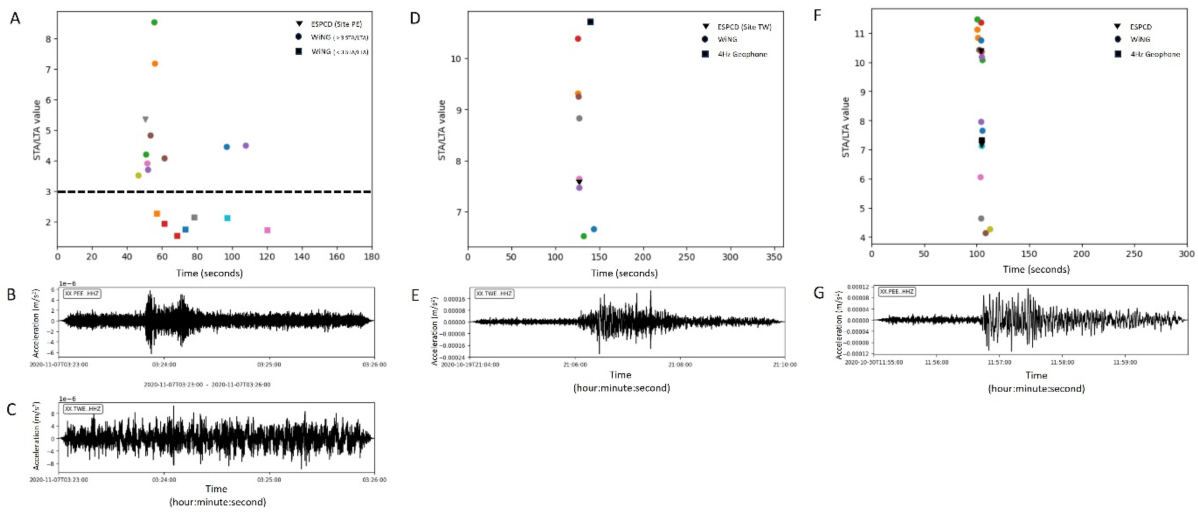

Figure 11. SSTA/LTA plots for a selection of earthquakes. A) MW 1.3 Stoke-on-Trent STA/LTA. B) Response of the 60s - 100 Hz ESPCD to the Stoke-on-Trent earthquake. C) Response of the 60s - 100 Hz ESPCD to the Stoke-on-Trent earthquake. D) MW 7.0 Greece STA/LTA; E) Response of the 60s - 100 Hz ESPCD to the Greece earthquake; F) MW 7.6 Alaksa STA/LTA; G) Response of the 60s - 100 Hz ESPCD to the Alaska earthquake.

This manifests in a poor-quality pick at several of the stations. However, there is a clear trend of picks at approximately 50 seconds, which clearly aligns with the ESPCD seismogram and demonstrates that an array of nodes can be utilised to detect earthquakes with relatively low amplitudes. The further two arrival plots are the Alaska (Figure 11D, E) and Greece (Figure 11 F, G) earthquake. The strong alignment of picks at 125s and 110s respectively demonstrate the quality of picking achieved by the WiNG nodes. The WiNG nodes also have comparable, and in some cases, higher STA/LTA values than the ESPCDs, suggesting a comparable signal-to-noise ratio. The performance of the nodes, and the abundance of nodes readily deployed within an array would clearly lend itself well to earthquake detection and location algorithms such as QuakeMigrate (Winder et al., 2020).

3.3.2 Crustal thickness estimate

Due to the short deployment time of only 28 days, there were only four earthquakes within 30°-90° epicentral distance from which to calculate receiver functions, and only one of these earthquakes produced an adequate receiver function (the Alaska earthquake of Figure 8). Nevertheless, both the ESPCD and the 3C-WiNG system recorded this earthquake and therefore a comparison between the ESPCD-derived RF and the WiNG-derived RF is possible (Figure 12).

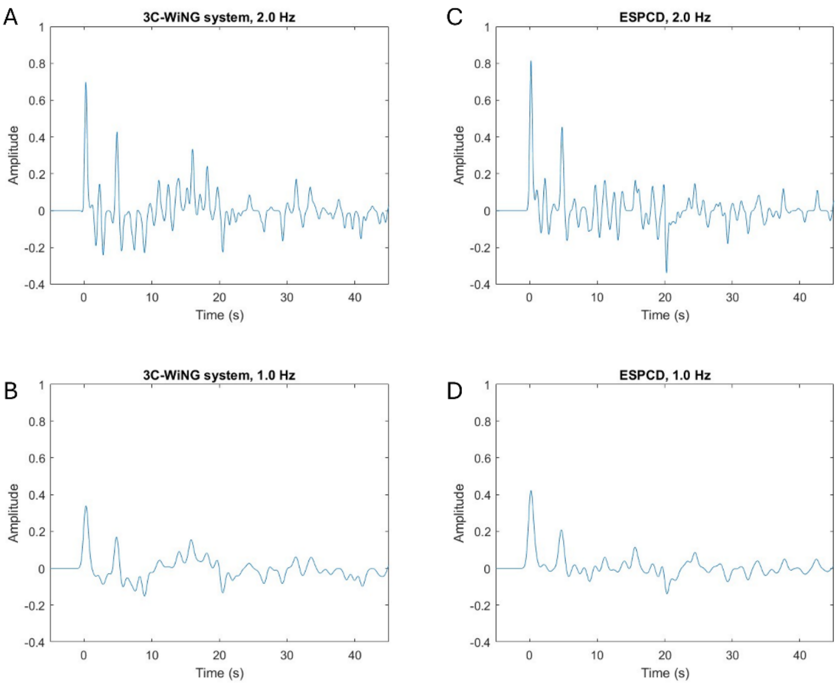

Figure 12. Receiver functions calculated for the MW 7.6 Alaska earthquake on 19th Oct. 2020. A) 2.0 Hz RF for the 3C-WiNG system. B) 1.0 Hz RF for the 3C-WiNG system. C) 2.0 Hz RF for the 60s - 100 Hz Güralp ESPCD. D) 1.0 Hz RF for the 60s - 100 Hz ESPCD.

The RFs are shown for both 1.0 Hz and 2.0 Hz, corresponding to a Gaussian width factor of 2.0 and 4.0 respectively. The WiNG-derived RF shows a strong similarity with the ESPCD-derived RF at each frequency, particularly within the 0 – 10s range. The ESPCD system provided a crustal thickness estimate of 37.9 ± 1.3 km and a Vp/Vs ratio of 1.78 ± 0.02 (Figure 13A), while the 3C-WiNG system provided a crustal thickness estimate of 39.0 ± 2.0 km and a Vp/Vs ratio of 1.77 ± 0.04 (Figure 13B).

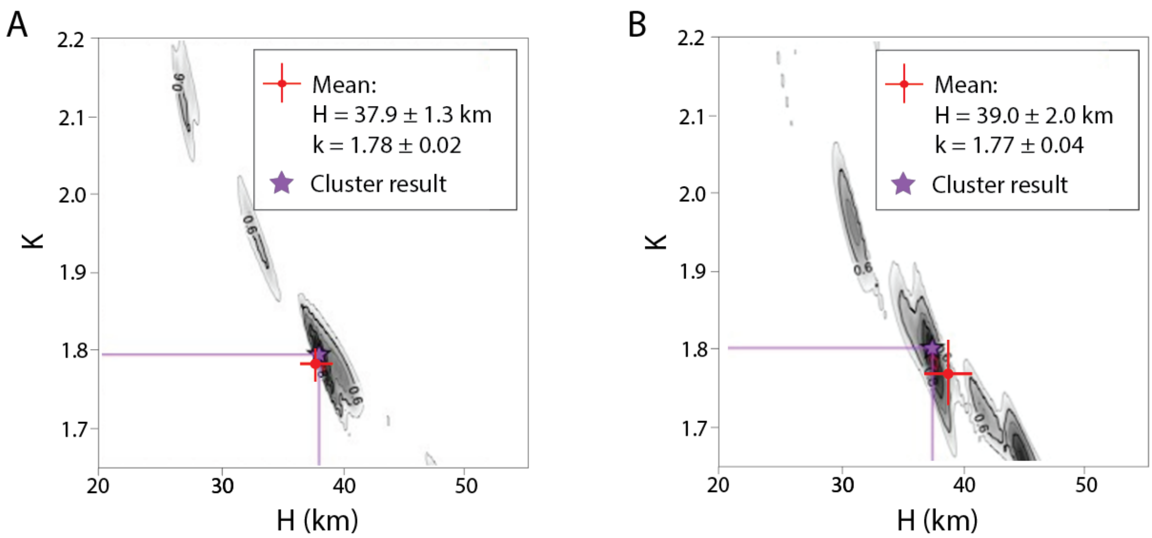

Figure 13. H-k stacking results. A) 60s - 100 Hz Güralp ESPCD. B) 3C-WiNG system.

These two estimates of crustal thickness both agree within error. Although these results are only based on a single earthquake, the values align well with the crustal thicknesses (36 – 39 km) and Vp/Vs ratios (1.72 – 1.77) calculated by Tomlinson et al. (2006) for the Midland Microcraton, on which Oxford lies.

4 Discussion

The MEMS sensor has been shown to record accurate information over a wide range of frequencies suitable for passive seismology. The self-noise of an instrument is a fundamental limit on its ability to record events. The WiNG nodes are characterised by a broadband noisefloor of -136dB for periods between 1s to 0.01 s. This is significantly below the NHNM, so signals within this frequency range will likely be recorded reliably. At periods above 1s, "flicker" noise with a slope of 1/*f* exceeds the broadband noise-floor and surpasses the NHNM at around 15 - 20s period. Consequently, it is possible that arrivals in this frequency range may be masked by the "flicker" noise. However, this study has shown that low-frequency surface waves from teleseismic earthquakes were well resolved in both time and frequency domain, with reliable measurement down to 30s. At periods less than 30s, the WiNG data compares well with that of the ESPCD (Figure 8). It should be noted that the WiNG nodes were all deployed in relatively water-rich topsoil, with only centimetre-scale burial, whereas the ESPCDs were directly buried in vaults ~1m deep. As such, the 30s limit may represent a coupling or damping issue and the low-frequency limit might improve at drier, firmer sites.

The random nature of the flicker noise also meant that cross-correlation techniques proved able to extract meaningful phase information from ambient surface waves travelling across the array, down to a period of 8s. Given the low-frequency performance of the WiNG nodes, the 8s limit of the ambient noise tomography is more than likely imposed by the relatively small instrument spacing within the array. It seems probable that the WiNG nodes could be used for regional and country-scale ambient noise and earthquake surface-wave tomography studies if an appropriate instrument spacing is used. The pseudo-3C WiNG system performed well for the receiver function analysis, providing a crustal thickness estimate within error of that achieved by the conventional ESCPD. The WiNG system had a larger error to its estimate, but that can largely be accounted for by the lack of rigid orthogonality and potential tilting provided for the 3 separate WiNG nodes (doubling as the three separate components) during the deployment. The manufacturer of the WiNG nodes has developed a metal stage to ensure orthogonality and reduce the effects of tilting. Given this, the WiNG nodes are certainly suitable for receiver function analysis.

The WiNG nodes, and other such nodal systems which rely on a MEMS accelerometer, have many clear advantages over the conventional seismometer systems. The nodes are significantly cheaper, costing £100s in comparison to the average ESPCD set-up costing £10,000s. The nodes can be deployed within a matter of minutes, versus a number of hours for the average ESPCD deployment. The nodes leave a far smaller surface footprint once deployed, which greatly helps with site security. The nodes are fully integrated so require no supporting equipment, and therefore provide a smaller logistical challenge when deploying a large array. The low cost, smaller size, and high speed of deployment means a large array of instruments can be deployed more easily and in a smaller time frame. However, the integrated nature of the nodal systems presents several disadvantages when compared with conventional seismometers. The internal GPS means that the node cannot be buried to a great depth because this would obscure the signal of the GPS. Geophones and ESPCDs rely on external GPS systems, meaning the seismometers can be buried at any depth and connected to a GPS on the surface. This increased depth of burial improves coupling with the ground, as can be seen by the higher amplitudes of the teleseismic arrivals in the ESPCD data when compared to the WiNG node data. The burial also shields the seismometer from signals of no interest, such as shallow anthropogenic noise. Finally, deep burial does make the seismometer more difficult to recover which can deter would-be thieves. The nodes also rely on an internal battery, which means that they can only record for a maximum of 50 days. For longer deployments, this means multiple trips into the field for re-charging. A final disadvantage of the MEMS sensor is the flicker noise below 1 Hz, which is an attribute of all electronic circuits. This means that low amplitude signals could be obscured by the noise-floor of the sensor, particularly at low-noise sites and especially at periods greater than 15 - 20s where the noise surpasses the NHNM.

5 Conclusions

This study has shown that the WiNG nodes reliably record over 100 Hz to 0.03 Hz, with a -136 dB broadband noise-floor between 100 – 1 Hz, and a $1/f$ noise-floor at frequencies below 1 Hz. The nodes accurately recorded a range of earthquakes, with a epicentral distances from 72°to 40 km. In particular, the low-period (c. 10 - 30s) surface waves of two teleseismic earthquakes were clearly resolved above the sensor's noise floor. The cross-correlation of pairs of nodes provided information on ambient surface waves down to periods of 8s, which provided sensitivity to seismic velocities down to a depth of 20 km. The 8s limit represents a limit enforced by the maximum station separations within the array and not the instruments themselves. A set of three WiNG nodes deployed in a 3-component configuration provided an accurate estimate of the crustal thickness beneath Oxford of 39.0

± 2.0 km using the H-k stacking technique on a calculated receiver function from a teleseismic MW 7.0 earthquake in Alaska. This estimate is in error of the estimate provided by the conventional 3-component ESPCD of 37.9 ± 1.3 km and aligns well with previous results in the literature. The nodal systems have a number of clear advantages over conventional systems, including speed of deployment, cost, small size. These advantages mean a large array of MEMS sensors could be deployed cheaply, easily and in a short time frame. The disadvantages include the restricted depth of burial, which reduces coupling and increases noise levels, and the limited life of the internal battery system. In conclusion, the strong performance of the WiNG nodes at frequencies above and below 1 Hz, in both ambient noise and earthquake analysis, shows that MEMS-based nodes are well-suited for passive seismology studies at a local, regional, and potentially larger scale.

Potential Conflicts of Interest

The Sercel WiNG nodes were deployed in partnership with Sercel.

Acknowledgements

We would like to thank Sercel for the donation of the Sercel WiNG nodal seismometers. Michael C. Daly would like to acknowledge funding from NERC CuBES WP1 Reference No. NE/T003170/1. Tobermory C. Mackay-Champion would like to thank BHP for generously funding his DPhil research.

Data Availability Statement

The data and codes for this project are available on Zenodo: 10.5281/zenodo.10909542.

References

Bensen, G.D. *et al.* (2007) 'Processing seismic ambient noise data to obtain reliable broad-band surface wave dispersion measurements', *Geophysical Journal International*, 169(3), pp. 1239–1260. Available at: https://doi.org/10.1111/j.1365-246X.2007.03374.x.

D'Alessandro, A., Luzio, D. and D'Anna, G. (2014) 'Urban MEMS based seismic network for post-earthquakes rapid disaster assessment', *Advances in Geosciences*, 40, pp. 1–9. Available at: https://doi.org/10.5194/adgeo-40-1-2014.

D'Alessandro, A., Scudero, S. and Vitale, G. (2019) 'A Review of the Capacitive MEMS for Seismology', *Sensors*, 19(14), p. 3093. Available at: https://doi.org/10.3390/s19143093.

Ekström, G., Nettles, M. and Dziewoński, A.M. (2012) 'The global CMT project 2004–2010: Centroid-moment tensors for 13,017 earthquakes', *Physics of the Earth and Planetary Interiors*, 200–201, pp. 1–9. Available at: https://doi.org/10.1016/j.pepi.2012.04.002.

Faber, K. and Maxwell, P. (1997) 'Geophone spurious frequency: What is it and how does it affect seismic data quality?', *Canadian Journal of Exploration Geophysics*, 3, pp. 46–54.

Fougerat, A., Guérineau, L. and Tellier, N. (2018) 'High-quality signal recording down to 0.001 Hz with standard MEMS accelerometers', in *SEG Technical Program Expanded Abstracts 2018*. Society of Exploration Geophysicists, pp. 196–200. Available at: https://doi.org/10.1190/segam2018-2995544.1.

Fuławka, K. *et al.* (2022) 'Application of MEMS-Based Accelerometers for Near-Field Monitoring of Blasting-Induced Seismicity', *Minerals*, 12(5), p. 533. Available at: https://doi.org/10.3390/min12050533.

Gerstoft, P., Fehler, M.C. and Sabra, K.G. (2006) 'When Katrina hit California', *Geophysical Research Letters*, 33(17). Available at: https://doi.org/10.1029/2006GL027270.

Halford, D. (1968) 'A general mechanical model for $|f|^{\alpha}$ spectral density random noise with special reference to flicker noise $1/|f|$', *Proceedings of the IEEE*, 56(3), pp. 251–258. Available at: https://doi.org/10.1109/PROC.1968.6269.

Harmon, N. *et al.* (2008) 'Phase velocities from seismic noise using beamforming and cross correlation in Costa Rica and Nicaragua', *Geophysical Research Letters*, 35(19). Available at: https://doi.org/10.1029/2008GL035387.

Harmon, N. and Rychert, C.A. (2016) 'Joint inversion of teleseismic and ambient noise Rayleigh waves for phase velocity maps, an application to Iceland', *Journal of Geophysical Research: Solid Earth*, 121(8), pp. 5966–5987. Available at: https://doi.org/10.1002/2016JB012934.

Havskov, J. and Alguacil, G. (2016) 'Seismic Sensors', in *Instrumentation in Earthquake Seismology*. Cham: Springer International Publishing, pp. 13–100. Available at: https://doi.org/10.1007/978-3-319-21314-9_2.

Herrmann, P. *et al.* (2021) 'Land Acquisition without Data Jitter Made Possible with MEMS Sensors', in *82nd EAGE Annual Conference & Exhibition*. European Association of Geoscientists & Engineers, pp. 1–5. Available at: https://doi.org/10.3997/2214-4609.202112510.

Herrmann, R.B. (2013) 'Computer Programs in Seismology: An Evolving Tool for Instruction and Research', *Seismological Research Letters*, 84(6), pp. 1081–1088. Available at: https://doi.org/10.1785/0220110096.

Kobayashi, N. and Nishida, K. (1998) 'Continuous excitation of planetary free oscillations by atmospheric disturbances', *Nature*, 395(6700), pp. 357–360. Available at: https://doi.org/10.1038/26427.

Koymans, M.R. *et al.* (2021) 'Performance Assessment of Geophysical Instrumentation Through the Automated Analysis of Power Spectral Density Estimates', *Earth and Space Science*, 8(9). Available at: https://doi.org/10.1029/2021EA001675.

Laine, J. and Mougenot, D. (2007) 'Benefits of MEMS Based Seismic Accelerometers for Oil Exploration', in *TRANSDUCERS 2007 - 2007 International Solid-State Sensors, Actuators and Microsystems Conference*. IEEE, pp. 1473–1477. Available at: https://doi.org/10.1109/SENSOR.2007.4300423.

Laine, J. and Mougenot, D. (2014) 'A high-sensitivity MEMS-based accelerometer', *The Leading Edge*, 33(11), pp. 1234–1242. Available at: https://doi.org/10.1190/tle33111234.1.

Ligorría, J.P. and Ammon, C.J. (1999) 'Iterative deconvolution and receiver-function estimation', *Bulletin of the Seismological Society of America*, 89(5), pp. 1395–1400. Available at: https://doi.org/10.1785/BSSA0890051395.

Liu, H.-F. *et al.* (2022) 'A review of high-performance MEMS sensors for resource exploration and geophysical applications', *Petroleum Science*, 19(6), pp. 2631–2648. Available at: https://doi.org/10.1016/j.petsci.2022.06.005.

Lognonné, P. *et al.* (2020) 'Constraints on the shallow elastic and anelastic structure of Mars from InSight seismic data', *Nature Geoscience*, 13(3), pp. 213–220. Available at: https://doi.org/10.1038/s41561-020-0536-y.

McNamara, D.E. and Buland, R.P. (2004) 'Ambient Noise Levels in the Continental United States', *Bulletin of the Seismological Society of America*, 94(4), pp. 1517–1527. Available at: https://doi.org/10.1785/012003001.

Ogden, C.S. *et al.* (2019) 'A reappraisal of the H–κ stacking technique: implications for global crustal structure', *Geophysical Journal International*, 219(3), pp. 1491–1513. Available at: https://doi.org/10.1093/gji/ggz364.

Peterson, J. (1993) *Observations and modeling of seismic background noise*.

Pike, W.T. *et al.* (2014) 'A self-levelling nano-g silicon seismometer', in *IEEE SENSORS 2014 Proceedings*. IEEE, pp. 1599–1602. Available at: https://doi.org/10.1109/ICSENS.2014.6985324.

Sleeman, R., van Wettum, A. and Trampert, J. (2006) 'Three-Channel Correlation Analysis: A New Technique to Measure Instrumental Noise of Digitizers and Seismic Sensors', *Bulletin of the Seismological Society of America*, 96(1), pp. 258–271. Available at: https://doi.org/10.1785/0120050032.

Tarantola, A. and Valette, B. (1982) 'Generalized nonlinear inverse problems solved using the least squares criterion', *Reviews of Geophysics*, 20(2), pp. 219–232. Available at: https://doi.org/10.1029/RG020i002p00219.

Tellier, N. and Herrmann, P. (2020) 'True Vertical and Orthogonal OBN Sensing with 3C MEMS Sensors', in *Second EAGE Marine Acquisition Workshop*. European Association of Geoscientists & Engineers, pp. 1–4. Available at: https://doi.org/10.3997/2214-4609.202034022.

Tellier, N., Laroche, S. and Herrmann, P. (2020) 'Native true amplitude and phase broadband sensing now available with the latest MEMS sensors', in *SEG Technical Program Expanded Abstracts 2020*. Society of Exploration Geophysicists, pp. 111–115. Available at: https://doi.org/10.1190/segam2020-3423114.1.

Tomlinson, J.P. *et al.* (2006) 'Analysis of the crustal velocity structure of the British Isles using teleseismic receiver functions', *Geophysical Journal International*, 167(1), pp. 223–237. Available at: https://doi.org/10.1111/j.1365-246X.2006.03044.x.

Wang, Y., Lin, F.-C. and Ward, K.M. (2019) 'Ambient noise tomography across the Cascadia subduction zone using dense linear seismic arrays and double beamforming', *Geophysical Journal International*, 217(3), pp. 1668–1680. Available at: https://doi.org/10.1093/gji/ggz109.

Winder, T. *et al.* (2019) 'QuakeMigrate: a Modular, Open-Source Python Package for Automatic Earthquake Detection and Location', in *American Geophysical Union, Fall Meeting*.

Woodcock, N. and Strachan, R. (2012) *Geological History of Britain and Ireland*. Wiley. Available at: https://doi.org/10.1002/9781118274064.

Zhu, L. and Kanamori, H. (2000) 'Moho depth variation in southern California from teleseismic receiver functions', *Journal of Geophysical Research: Solid Earth*, 105(B2), pp. 2969–2980. Available at: https://doi.org/10.1029/1999JB900322.

Figure captions:

Figure 1: Deployment map. The BGS 1:50K EW236 Whitney Bedrock map is reproduced with the permission of the British Geological Survey © UKRI 2023. All Rights Reserved.

Figure 2: Deployment techniques for the WiNG nodes.

Figure 3: Instrument response Bode plot. (A) WiNG nodes. (B) GS-11D 4.5Hz geophone and RefTek DAS130-01 broadBand data logger. (C) 60s - 100 Hz Güralp CMG-ESPCD.

Figure 4: Probabilistic Power Spectral Density analysis on 5th November 2020. A) WiNG node. B) Geophone. C) ESPCD. Each instrument has a sampling frequency of 250 Hz in units of acceleration for this analysis. The solid black lines are the New High Noise Model (top) and New Low Noise Model (bottom) of Peterson (1993).

Figure 5: A) One-side cross-correlation moveout. The blue line corresponds to a velocity of 3 km/s. B) Array beamforming surface wave dispersion.

Figure 6: 2D phase velocity maps. A) Phase velocity map of 2.5s wave. B) Error in the phase velocity measurements at 2.5s. C) Phase velocity map of 5.5s wave. D) Error in the phase velocity measurements at 5.5s.

Figure 7: 1D S-wave inversion. A) The observed dispersion curve, and the forward modelled

dispersion curve. B) The resulting S-wave velocity profile. C) The depth sensitivity of the surface waves used in the inversion.

Figure 8: Instrument response to a MW 7.6 Alaska earthquake on 19th Oct. 2020. A) Instrument Power Spectral Density, in units of acceleration decibels relative to 1. (B, C, D, E, F) ESPCD acceleration data with a 1 s, 10 s, 20 s, 30 s and 40 s low-pass filter, respectively. (G, H, I, J, K) WiNG node acceleration data with a 1 s, 10 s, 20 s, 30 s and 40 s low-pass filter, respectively. (L, M, N, O, P) 4.5 Hz geophone acceleration data with a 1 s, 10 s, 20 s, 30 s and 40 s low-pass filter, respectively.

Figure 9: The response of the WiNG node array to the Greece Earthquake (MW 7.0), 30th Oct. 2020. A bandpass filter of 0.05 - 1 Hz has been applied. The blue plots correspond to nodes that were buried underground. The red plots correspond to nodes that were spiked into the ground.

Figure 10: Response of the WiNG node to a selection of earthquakes. A) WiNG node response to the MW 2.7 North Sea earthquake; B) A continuous-wavelet-transform analysis of the North Sea earthquake. C) PPSD analysis of 30th Oct. 2020, featuring the MW 7.0 Greece earthquake; D) WiNG node response to the MW 0.9 Worcester earthquake; E) A continuous-wavelet-transform analysis of the Worcester earthquake; F) PPSD analysis of 19th Oct. 2020, featuring the MW 7.6 Alaska earthquake MW 7.6 Alaska.

Figure 11: STA/LTA plots for a selection of earthquakes. A) MW 1.3 Stoke-on-Trent STA/LTA. B) Response of the 60s - 100 Hz ESPCD to the Stoke-on-Trent earthquake. C) Response of the 60s - 100 Hz ESPCD to the Stoke-on-Trent earthquake. D) MW 7.0 Greece STA/LTA; E) Response of the 60s - 100 Hz ESPCD to the Greece earthquake; F) MW 7.6 Alaksa STA/LTA; G) Response of the 60s - 100 Hz ESPCD to the Alaska earthquake.

Figure 12: Receiver functions calculated for the MW 7.6 Alaska earthquake on 19th Oct. 2020. A) 2.0 Hz RF for the 3C-WiNG system. B) 1.0 Hz RF for the 3C-WiNG system. C) 2.0 Hz RF for the 60s - 100 Hz Güralp ESPCD. D) 1.0 Hz RF for the 60s - 100 Hz ESPCD.

Figure 13: H-k stacking results. A) 60s - 100 Hz Güralp ESPCD. B) 3C-WiNG system.